Quantitative evaluation of two scatter correction techniques for ^{18}F-FDG brain PET/MR imaging in regard to MR-based attenuation correction

Jarmo Teuho[1,2], Virva Saunavaara[2,3], Tuula Tolvanen[2,3], Terhi Tuokkola[2], Antti Karlsson[3,4], Jouni Tuisku[2], Mika Teräs[3,5]

1. Turku PET Centre, University of Turku, Turku, Finland

2. Turku PET Centre, Turku University Hospital, Turku, Finland

3. Department of Medical Physics, Turku University Hospital, Turku, Finland

4. Turku Centre for Quantum Physics, Department of Physics and Astronomy, University of Turku, Turku, Finland

5. Institute of Biomedicine, University of Turku, Turku, Finland

Correspondence: Jarmo Teuho,

Turku PET Centre, c/o Turku University Hospital,

Kiinamyllynkatu 4-8, 20520 Turku, Finland.

Ph: +358407741366, Fax: +3582231 8191,

email: jarmo.teuho@tyks.fi

First author: Jarmo Teuho, Doctoral candidate,

Turku PET Centre, c/o Turku University Hospital,

Kiinamyllynkatu 4-8, 20520 Turku, Finland.

Ph: +35840774 1366, Fax: +35822318191,

email: jarmo.teuho@tyks.fi

Word count: 5000

Running title: Scatter correction techniques in PET/MR

ABSTRACT

In positron emission tomography (PET), corrections for photon scatter and attenuation are essential for visual and quantitative consistency. Magnetic resonance attenuation correction (MRAC) is generally conducted by image segmentation and assignment of discrete attenuation coefficients, which offers limited accuracy compared to computed tomography attenuation correction (CTAC). Potential inaccuracies in MRAC may affect scatter correction, as the attenuation image (μ-map) is used in single scatter simulation (SSS) to calculate the scatter estimate. We assessed the impact of MRAC to scatter correction by using two scatter correction techniques and three μ-maps for MRAC. **Methods:** The SSS and a Monte Carlo – based single scatter simulation (MCSSS) algorithm implementations on the Philips Ingenuity TF PET/MR were used with one CT-based and two MR-based μ-maps. Data from seven subjects were used in the clinical evaluation while a phantom study using an anatomical brain phantom was conducted. Scatter correction sinograms were evaluated for each scatter correction method and μ-map. Absolute image quantification was investigated with the phantom data. Quantitative assessment of PET images was performed by volume of interest (VOI) and ratio image analysis. **Results:** MRAC did not result in large differences in scatter algorithm performance, especially with SSS. Scatter sinograms and scatter fractions did not reveal large differences regardless of the μ-map used. SSS showed slightly higher absolute quantification. The differences in VOI analysis between SSS and MCSSS were 3 % at maximum in the phantom and 4 % in the patient study. Both algorithms showed excellent correlation with each other with no visual differences between PET images. MCSSS showed a slight dependency on the μ-map used, with difference of 2 % on average and 4 % at maximum when using a μ-map without bone. **Conclusion:** The effect of different MR-based μ-maps to the performance of scatter correction was minimal in non-time-of-flight (TOF) ^{18}F-FDG PET/MR brain imaging. The SSS algorithm was not affected significantly by MRAC. The performance of MCSSS algorithm is comparable but not superior to SSS, warranting further investigations of algorithm optimization and performance with different radiotracers and TOF imaging.

Keywords: PET/MR, scatter correction, attenuation correction, image quantification

INTRODUCTION

In brain PET/MR imaging, accurate scatter and attenuation correction are essential for image quality and quantitative accuracy of reconstructed PET images. Scatter and attenuation correction are closely connected as emission and attenuation images are used to estimate the amount of scattered photons in SSS, which relies on the accuracy of the estimated emission images and the μ-map (*1*). Therefore, the accuracy of the μ-map will also contribute to performance of SSS. However, only limited investigations have been performed about the effect of the accuracy of the μ-map to performance of SSS in PET/MR imaging (*2*).

In PET/MR imaging, the accuracy of the μ-map is limited in MRAC compared to CTAC. As linear attenuation coefficients cannot be measured from MR images as in CT, photon attenuation needs to be estimated by other means, commonly by image segmentation (*3*). The resulting MR-based μ-map will inherently be an approximation of the true attenuation. As this μ-map is used in scatter correction, inconsistencies in PET image quantification may result. Therefore, it is critical to investigate the effect of MRAC to the performance of current scatter correction techniques for brain PET/MR imaging with different μ-maps (*2*).

In the Philips Ingenuity TF PET/MR, scatter correction can be applied by two techniques: the SSS and the MCSSS. The main difference between the algorithms is how the scaling factors are derived for matching the scatter sinogram to measured emission data. The scaling is performed either by tail fitting (SSS) or low-count Monte Carlo (MC) simulation (MCSSS) (*4*). A short description of vendor-specific implementations of SSS and MCSSS algorithms is given below.

The SSS algorithm models the contribution of single scatter events where an annihilation photon has been scattered only once (*1,2,4-8*). It is assumed that total scatter including single and multiple scatter can be derived from a scaled distribution of single scatter. (*1,2,4-8*). The scatter estimate needs to be scaled to match the emission data, where scaling is implemented as a linear transformation (*1,2,4-8*). The scaling parameters can be derived by fitting SSS data with a least-mean-squares technique to the scatter tails of the emission data (tail fitting) (*1,2,4-8*). The tail part of the scatter sinogram is determined by deriving a mask from the attenuation correction sinogram. The tails correspond to the emission lines of response that do not pass through the object,

representing pure scatter (*1,2,4-8*). After tail fitting, the scaled scatter distribution is subtracted from the normalized emission data (*1,2,4-8*). This vendor-specific version of the SSS is considered an accurate and computationally efficient technique for scatter correction.

MCSSS is a novel approach, using a combination of SSS and low-count MC simulation to derive the scaling parameters instead of tail fitting (*4*). The scatter contribution shape is realized by SSS and the scaling factor is determined by a MC simulation to match the SSS sinogram to the emission data (*4*). As the scaling factors are derived by a MC simulation, the accuracy of the scaling parameters is not dependent on the quality of tail fitting. This can be considered to be an advantage of the MCSSS algorithm over SSS. However, initial evaluations of MCSSS have been performed only for whole-body imaging, with no implications or thorough regional analysis performed for brain in PET/MR imaging (*4,9*), where the effect of MRAC is more pronounced, especially when ignoring bone. Therefore, evaluation of the MCSSS algorithm for brain PET/MR imaging is warranted.

Our aim was to evaluate the effect of MRAC to two scatter correction techniques in brain PET/MR with three methods for MRAC. We hypothesized that the scatter correction techniques should be largely unaffected by the inaccuracies of MRAC in static ^{18}F-FDG brain imaging and would not expect large differences in quantitative performance in clinical scan conditions. While MRAC in PET/MR imaging has been studied extensively (*3*), there are no known clinical reports on the performance of scatter algorithms with different methods for MRAC.

MATERIALS AND METHODS

Patient population

The study protocol was approved by an institutional review board (Ethics Committee), the radiation protection authorities and was performed according to the latest version of the Declaration of Helsinki. All subjects signed a written informed consent form. Subjects who had undergone PET/MR and PET/CT examination during the same day with a single-injection and dual-imaging protocol were included in the patient material. All patients had been referred to our institute for a clinical routine PET/CT ^{18}F-FDG PET brain

examination with an additional PET/MR examination. The CTAC data from the PET/CT examination was used in the evaluation as a reference method for PET/MR attenuation correction. The clinical data included seven subjects (3 male and 4 female) with median and range of age and weight: 47 (26-74) years and 77 (47-80) kg. A patient with a metal implant was included in the study.

PET/MR and PET/CT imaging protocol

All subjects had undergone a PET/MR (Ingenuity TF PET/MR, Philips Healthcare, Cleveland, OH, USA) and a PET/CT (Discovery 690 PET/CT, General Electric Healthcare, Milwaukee, WI, USA) examination performed in a randomized fashion. The physical performance of both systems is described in (*10,11*). Patients were administered ^{18}F-FDG depending on their body weight. The median dose and range were 274 (199-299) MBq, while mean ± standard deviation of the first PET scan start times were 80 ± 20 minutes post-injection. The PET/CT and PET/MR examinations were conducted using the standard protocol for neuroimaging at our institute.

The PET/MR imaging consisted of T1-weighted 3D Fast Field Echo for clinical MRAC followed by a PET examination. An 8-channel head coil was used for MR imaging. The parameters for MRAC were: echo time 2.16 ms, repetition time 4.18 ms, flip angle 10 degrees, field of view of 320 mm and acquisition time of 84 seconds. The PET acquisition was performed with a transaxial field of view of 256 mm, over one bed position covering the entire head region, with duration of 15 minutes.

At the PET/CT, a low-dose CTAC with tube voltage of 120 kV using automatic dose modulation with 10 mAs was acquired and was used as the reference method for PET/MR attenuation correction in this study.

3D brain phantom imaging protocol

A phantom scan was performed to complement the patient data. A standard NEMA scatter phantom and a 3D printed anatomical brain phantom (Iida phantom) were used (*12*). The NEMA scatter phantom was placed approximately 8 cm apart from the brain phantom to simulate scatter originating from the

patient body in a clinical brain scan. Phantoms were fixed by straps to prevent motion in the MR and PET scans. Foam pads were used to support the phantom head on the bed.

The phantom measurements were done on the same PET/MR and PET/CT systems as the patient scans, using a similar scan protocol for PET, MR and CT. All PET scans were performed in list-mode, with scan duration of 15 minutes without a head coil on the PET/MR. Afterwards; the phantom was transferred to the PET/CT, where a standard low-dose CTAC using a tube voltage of 120 kV was collected for reference method for PET/MR attenuation correction.

The brain phantom gray matter compartment was filled with 40 MBq of radioactivity in 750 ml of water while the NEMA scatter phantom was filled with 105 MBq of radioactivity from the same batch. The brain phantom skull compartment was filled with a K_2HPO_4 solution supplied with the phantom, with a concentration of 100 g of salts in 67 g of water. A gamma counter (1480 Wizard 3", Perkin Elmer, Turku, Finland) was used to determine the absolute activity concentration in the brain phantom at the PET/MR scan start time. Finally, the attenuation coefficient (μ-value) of the phantom skull was measured from the acquired CT images.

MR-based and CT-based attenuation correction for phantom and patients

Three μ-maps of were used to evaluate the effect MRAC to the performance of scatter correction in both the phantom and patient study. For MRAC, a 3-class μ-map ($MRAC_{3class}$) and a 2-class μ-map ($MRAC_{2class}$) were used. The $MRAC_{3class}$ consisted of soft tissue, air and bone, while $MRAC_{2class}$ included only soft tissue and air. CTAC was used as the reference μ-map. The μ-values for the MR-based μ-maps in the patient study were assigned as follows: air (0.0 cm^{-1}), soft tissue (0.096 cm^{-1}) and bone (0.151 cm^{-1}) (13).

$MRAC_{3class}$ and $MRAC_{2class}$ for patients were created using a method described in (14). $MRAC_{3class}$ was created similarly to (14) while $MRAC_{2class}$ was created by replacing the skull μ-values with soft tissue, ignoring the patient skull. For CTAC, the head of each subject was carefully segmented out by semi-automatic regional contouring tools in Carimas 2.8 (Turku PET Centre, Turku, Finland). Thereafter, the CT Hounsfield unit values were converted to μ-values by a bi-linear transformation (15).

For the phantom, MR-based μ-maps were created using MATLAB2011b (Mathworks Inc. Natick, US) and in-house software. MRAC$_{2class}$ was created by assigning a μ-value of soft tissue for the entire phantom volume segmented from CTAC. In MRAC$_{3class}$, bone was added by segmentation the phantom skull from the CTAC and assignment of a discrete μ-value of bone to the region of the skull. The bone was assigned a μ-value of 0.128 cm^{-1}, as measured from the CT scan. CT-based μ-maps were created by segmenting out the phantom from the CTAC and by conversion of Hounsfield unit values to μ-values (*15*).

Finally, μ-maps were registered to non-attenuation corrected PET images for best possible registration before image reconstruction. All images were smoothed to PET resolution of 5 mm as in (*16*). Example μ-maps of the phantom and one subject are presented in (Fig. 1).

PET image reconstruction and scatter correction

PET images were reconstructed using SSS and MCSSS. For both scatter correction methods, three μ-maps were used: CTAC, MRAC$_{3class}$ and MRAC$_{2class}$. All reconstruction parameters were fixed between SSS and MCSSS reconstructions. Reconstructions were performed using LOR-RAMLA with 3 iterations and 33 subsets, matrix size of 128x128x90 and voxel size of 2 mm. Neither TOF nor resolution modelling were applied due to technical limitations in the reconstruction system.

All reconstructions included the necessary corrections for image quantification: randoms, scatter, dead-time, decay and detector normalisation. Reconstructions of the clinical subjects included the head coil template and the patient table, inserted automatically by reconstruction software. The phantom image reconstructions included only the patient table since no head coil was present.

SSS and MCSSS scatter sinogram analysis

Sinograms from SSS and MCSSS were extracted from the PET reconstruction system. The randoms-corrected emission, transmission and the final scatter sinogram from SSS and MCSSS were extracted. Sinogram radial profiles were then inspected. The profiles were averaged over all tilt angels (N=7) and drawn over central axial bin and phi angle.

For each method, the total scatter fraction (SF_{total}) from the measured sinogram data for the phantom and subjects was calculated as:

$$SF_{total} = \sum_{i=0}^{n} Events_{scatter} / \sum_{i=0}^{n}(Events_{prompt} - Events_{delay}) \qquad (1)$$

, where ($Events_{scatter}$) is the scatter sinogram, ($Events_{prompt}$) the prompt sinogram and ($Events_{delay}$) is the delay sinogram.

Quantitative evaluation of phantom PET images

Quantitative assessment of absolute activity recovery in addition to regional VOI assessment was performed to the phantom PET images. Absolute activity recovery was measured with a single VOI covering the gray matter volume and with eight anatomical VOI from CTAC reconstructed PET images. Thereafter, the radioactivity from phantom PET images (Activity$_{measured}$) was measured and the recovery coefficient (%RC) against the value measured from the gamma counter (Activity$_{calibrator}$) was calculated:

$$\%RC = Actvity_{measured} / Activity_{calibrator} * 100 \qquad (2)$$

The phantom VOI analysis was performed similarly to our previous study (*17*). In the analysis, the phantom PET images were co-registered and re-sliced to a reference volume using rigid registration on SPM8 (Wellcome Trust Centre for Neuroimaging, University College London, UK). The reference volume size was 140x140x140 pixels with 1.22 mm isotropic resolution. Thereafter, a 5 mm Gaussian post-filter was applied to negate image noise. An anatomical 3D VOI set created previously (*17*) was used to measure radioactivity concentration in one deep brain and seven cortical regions.

The mean relative difference %Δ between SSS and MCSSS from equation (3) was calculated for each VOI and μ-map as follows:

$$\%\Delta = (PET_{MCSSS} - PET_{SSS}) / PET_{SSS} \qquad (3)$$

Where PET$_{MCSSS}$ denotes the activity measured from MCSSS, while PET$_{SSS}$ denotes the activity measured from SSS.

Quantitative PET image evaluation of the clinical subjects

PET images were evaluated quantitatively by VOI assessment of regional radioactivity and by ratio image analysis for visualizing regional differences. The quantitative analysis was performed by using MATLAB2011b and SPM8.

VOI analysis was performed automatically, employing an anatomical atlas from automated anatomical labelling software (*18*), using 35 cortical VOI (Supplemental Table 1) in the brain. Individualization of the atlas was based on the spatial mapping from the Montreal Neurological Institute space to individual space using Unified Segmentation in SPM8. The atlas image was masked in the individual space using summed tissue probability maps from Unified Segmentation from gray matter, white matter and cerebrospinal fluid with a lower threshold of 0.5.

The relative difference between SSS and MCSSS reconstructed PET images was assessed. The mean relative difference %Δ between SSS and MCSSS, with regional standard deviation were calculated for each VOI and for each μ-map used in PET reconstruction from equation (3). Linear regression analysis of MCSSS versus SSS reconstructed PET activity values was performed for 35 VOIs in both left and right hemisphere over 7 patients, totaling 490 points

Additionally, pixel-by-pixel ratio images were derived by equation (3), from which mean ratio images across all subjects were calculated for both algorithms and all μ-maps. Finally, mean PET images across all subjects were calculated using SPM8.

RESULTS

Sinogram profiles from the phantom and the clinical subjects are presented in (Figs. 2 and 3). Additional profiles are presented in (Supplemental Figs. 1 and 2). A minor difference can be seen when using MCSSS, where CTAC has the highest and $MRAC_{2class}$ has the lowest scatter profile. There is virtually no difference in the scatter sinogram profiles with SSS.

SF_{total} from equation (1) in the phantom study for SSS was 19.25% with CTAC, 19.24% with MRAC$_{3class}$ and 19.23% with MRAC$_{2class}$. SF_{total} for MCSSS was 19.95% with CTAC, 18.35% with MRAC$_{3class}$ and 17.84% with MRAC$_{2class}$. SF_{total} from equation (1) for individual subjects with SSS or MCSSS is presented in Table 1: Only minor differences were detected with the SSS algorithm.

Table 2 shows the results from the absolute activity measurement of the phantom with a whole brain VOI while Table 3 shows the calculated %RC in individual VOI when using CTAC. The %RC was calculated using a value of 45.87 kBq/ml for true activity.

Table 4 shows the results from the individual VOI analysis of the phantom study between SSS and MCSSS reconstructed PET for each μ-map.

The VOI analysis results of the clinical subjects are presented in (Fig. 4). Additional analysis is presented in (Supplemental Fig. 3). The mean difference between SSS and MCSSS reconstructed PET is smaller than 2.1 % while the maximum difference is 4.2 %.

(Fig. 5) shows linear regression analysis results between SSS and MCSSS reconstructed PET.

(Fig. 6) shows mean PET ratio images of SSS versus MCSSS reconstructed PET over all subjects with each μ-map.

Finally, (Fig. 7) shows mean PET images over all subjects, showing a visual comparison of SSS and MCSSS reconstructed PET with different μ-maps.

DISCUSSION

An evaluation of two scatter correction techniques with different μ-maps for MRAC in ^{18}F-FDG PET/MR brain imaging was performed. Investigation of scatter sinograms, scatter fractions, regional quantification and cross-correlation of reconstructed activity was performed. Two scatter correction techniques were compared with a brain phantom and clinical subjects using three μ-maps in a clinical PET/MR system, for the first time.

Differences between SSS and MCSSS were minimal in the sinogram profiles (Figs. 2 and 3) and scatter fractions in the phantom and patient study, regardless of the μ-map used in PET reconstruction. SF_{total} remained mostly unchanged with SSS while MCSSS showed the lowest SF_{total} when using MRAC$_{2class}$ both in the phantom and patient study. This difference in SF_{total} was 2 % in the phantom study and 4 % in the patient study.

Quantitatively, the absolute activity recovery and VOI analysis of the phantom showed minor differences between SSS and MCSSS regardless of the μ-map (Table 2, 3 and 4). Differences in whole-brain activity and %RC were minimal (Table 2). In VOI analysis, SSS showed a slightly higher %RC than MCSSS (Table 3). The mean difference between SSS and MCSSS in the phantom was 2.51 % at maximum, in one background region with MRAC$_{2class}$ (Table 4). Thus, the quantitative performance of MCSSS was comparable but not superior to SSS (Tables 2 and 3).

Similarly, minor differences between SSS and MCSSS were detected in the patient VOI analysis, regardless of the μ-map. The difference was 2 % on average and 4 % at maximum (Fig. 4). Largest differences existed with MRAC$_{2class}$. Excellent correlation ($R^2>0.99$) was found between SSS and MCSSS reconstructed PET regardless of the μ-map (Fig. 5).

In MCSSS a positive bias was detected which was highest with the μ-map that ignores bone (Figs. 4 and 6). In terms of final scatter fractions (4 % difference) and quantitative analysis (2 % mean difference), this bias can be considered to be clinically insignificant. These differences could not also be detected visually (Fig. 6). Ye et al. compared SSS and MCSSS visually with phantom and patient data in the body, concluding that both algorithms have similar visual appearance in the absence of scatter correction artifacts (*4*).

Therefore, our study implies that scatter algorithm performance is not affected significantly by imperfections in MRAC, especially with the SSS algorithm. The performance of both algorithms remained virtually unchanged regardless of the μ-map used in the PET image reconstruction. The influence of MRAC might be small on SSS implementations of other vendors as well, as highly undersampled emission and attenuation images are commonly used in SSS. Similarly to our study, Bourgos et al concluded that the

12

difference between an ideal scatter estimate with CTAC and non-ideal with MRAC was less than 1 % with SSS algorithm in a simulation study (*2*).

Thus, the SSS algorithm remains a reliable method for scatter correction. We could not detect a specific advantage in preferring MCSSS over SSS for clinical non-TOF ^{18}F-FDG brain imaging. There are specific conditions where another scatter correction technique might be preferred over SSS. These include head motion between emission and transmission (MRAC) (*6*), large signal voids in MRAC due to implants, a high-activity radiotracer e.g. O-15 (*19*).

A limitation is that only vendor-specific implementations of SSS and MCSSS were studied. Additionally, scatter algorithm performance should be investigated using TOF or radiotracers with more complex uptake than ^{18}F-FDG. Such studies are highly encouraged as scatter estimation is expected to be more challenging for tracers with specific uptake (e.g ^{11}C-Raclopride). Finally, the effect of scatter and attenuation correction in PET/MR to kinetic parameters as in (*7*) would be of interest.

CONCLUSION

The effect of MRAC to the performance of scatter correction algorithms was minimal in non-TOF ^{18}F-FDG brain PET/MR imaging. The SSS algorithm offered consistent quantitative performance regardless of the accuracy of the MR-based μ-map. The performance of MCSSS algorithm was comparable but not superior to SSS, warranting for further investigations of algorithm optimization and performance with different radiotracers and TOF imaging.

ACKNOWLEDGMENTS

CONFLICT OF INTEREST

The authors have no conflicts of interest to declare.

REFERENCES

(1)   Watson CC. New, faster, image-based scatter correction for 3D PET. *IEEE Trans Nucl Sci*. 2000;47:1587–1594.

(2)   Burgos N, Thielemans K, Cardoso MJ, et al. Effect of scatter correction when comparing attenuation maps: application to brain PET/MR. *IEEE Nuclear Science Symp Conf Record*. 2014;1-5.

(3)   Mehranian A, Arabi H, Zaidi H. Vision 20/20: magnetic resonance imaging-guided attenuation correction in PET/MRI: challenges, solutions, and opportunities. *Med Phys*. 2016;43:1130–1155.

(4)   Ye J, Song X, Hu Z. Scatter correction with combined single-scatter simulation and Monte Carlo simulation for 3D PET. *IEEE Nuclear Science Symp Conf Record*. 2014;1-3.

(5)   Accorsi R, Adam L-E, Werner ME, Karp JS. Optimization of a fully 3D single scatter simulation algorithm for 3D PET. *Phys Med Biol*. 2004;49:2577–2598.

(6)   Anton-Rodriguez JM, Sibomana M, Walker MD, et al. Investigation of motion induced errors in scatter correction for the HRRT brain scanner. *IEEE Nuclear Science Symp Conf Record*. 2010;2935–2940.

(7)   Mansor S, Boellaard R, Huisman MC, et al. Impact of new scatter correction strategies on high-resolution research tomograph brain PET studies. *Mol Imaging Biol*. 2016;18:627–635.

(8)   Wang W, Hu Z, Gualtieri EE, et al. Systematic and distributed time-of-flight list mode PET reconstruction. *IEEE Nuclear Science Symp Conf Record*. 2006;1715–1722.

(9)   Teuho J, Johansson J, Linden J, Saunavaara V, Teräs M. Comparison of single-scatter simulation and Monte Carlo single-scatter simulation on Philips Ingenuity TF PET/MR. *IEEE Nuclear Science Symp Conf Record*. 2014; 1-3.

(10)   Zaidi H, Ojha N, Morich M, et al. Design and performance evaluation of a whole-body Ingenuity TF PET–MRI system. *Phys Med Biol*. 2011;56:3091–3106.

(11)   Bettinardi V, Presotto L, Rapisarda E, Picchio M, Gianolli L, Gilardi MC. Physical performance of the new hybrid PET/CT Discovery-690. *Med Phys.* 2011;38:5394–5411.

(12)   Iida H, Hori Y, Ishida K, et al. Three-dimensional brain phantom containing bone and grey matter structures with a realistic head contour. *Ann Nucl Med.* 2013;27:25–36.

(13)   Catana C, van der Kouwe A, Benner T, et al. Toward implementing an MRI-based PET attenuation-correction method for neurologic studies on the MR-PET brain prototype. *J Nucl Med.* 2010;51:1431–1438.

(14)   Teuho J, Linden J, Johansson J, Tuisku J, Tuokkola T, Teräs M. Tissue probability-based attenuation correction for brain PET/MR by using SPM8. *IEEE Trans on Nucl Sci.* 2016;63:2452–2463.

(15)   Burger C, Goerres G, Schoenes S, Buck A, Lonn AHR, Von Schulthess GK. PET attenuation coefficients from CT images: experimental evaluation of the transformation of CT into PET 511-keV attenuation coefficients. *Eur J Nucl Med Mol Imaging.* 2002;29:922–927.

(16)   Schramm G, Langner J, Hofheinz F, et al. Quantitative accuracy of attenuation correction in the Philips Ingenuity TF whole-body PET/MR system: a direct comparison with transmission-based attenuation correction. *MAGMA.* 2013;26:115–126.

(17)   Teuho J, Johansson J, Linden J, et al. Effect of attenuation correction on regional quantification between PET/MR and PET/CT: a multicenter study using a 3-dimensional brain phantom. *J Nucl Med.* 2016;57:818–824.

(18)   Tzourio-Mazoyer N, Landeau B, Papathanassiou D, et al. Automated anatomical labeling of activations in SPM using a macroscopic anatomical parcellation of the MNI MRI single-subject brain. *Neuroimage*. 2002;15:273–289.

(19)   Hori Y, Hirano Y, Koshino K, et al. Validity of using a 3-dimensional PET scanner during inhalation of 15O-labeled oxygen for quantitative assessment of regional metabolic rate of oxygen in man. *Phys Med Biol.* 2014;59:5593–5609.
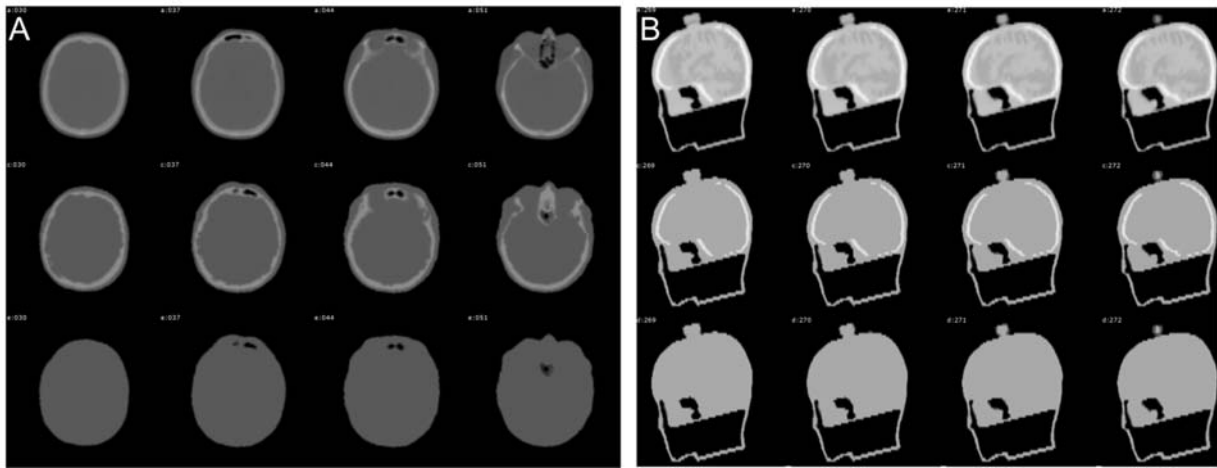
FIGURE 1. Visualization of CT- and MR-based μ-maps of a clinical subject (A) and the phantom (B). The CT-based μ-maps are presented in 1st row, while MRAC$_{3class}$ and MRAC$_{2class}$ μ-maps are presented in 2nd and 3rd row. The window level between the μ-maps is set the same.
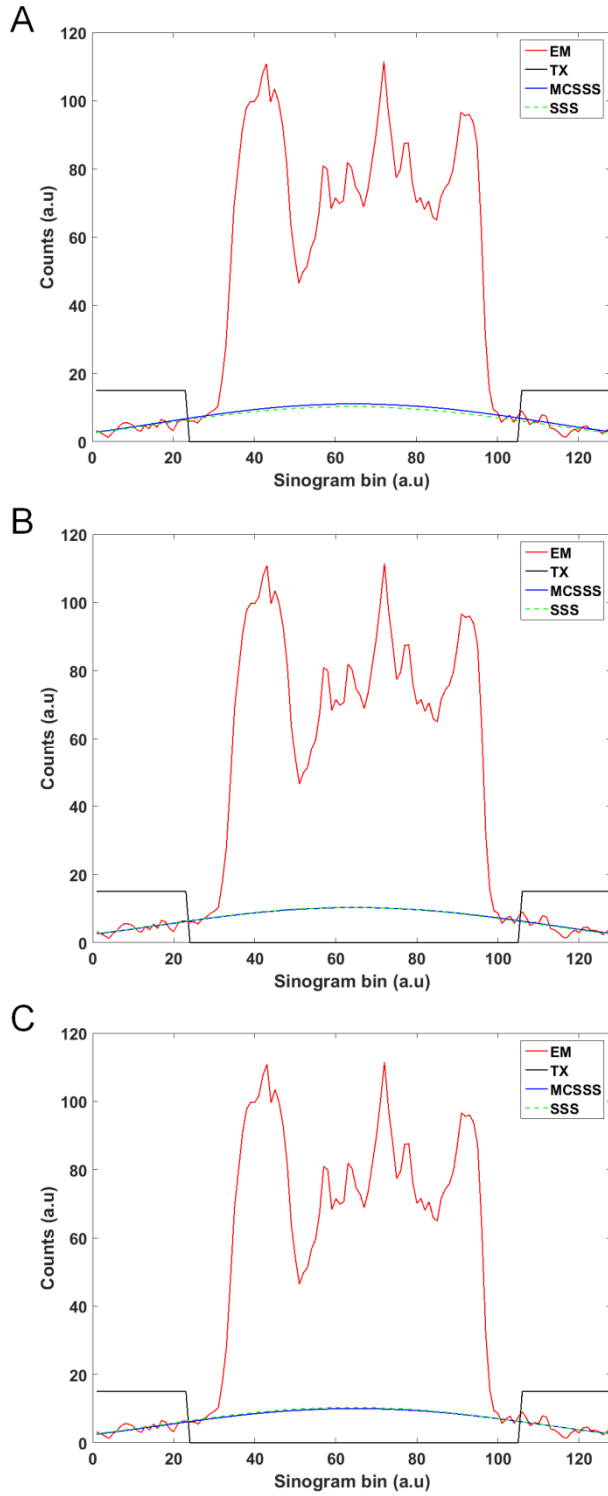
FIGURE 2. Measured sinogram profiles from randoms-corrected emission sinogram (EM) transmission sinogram mask (TX) and scatter correction sinograms from SSS and MCSSS for the phantom. (A), (B) and (C) show CTAC, $MRAC_{3class}$ and $MRAC_{2class}$ reconstructed PET, respectively.
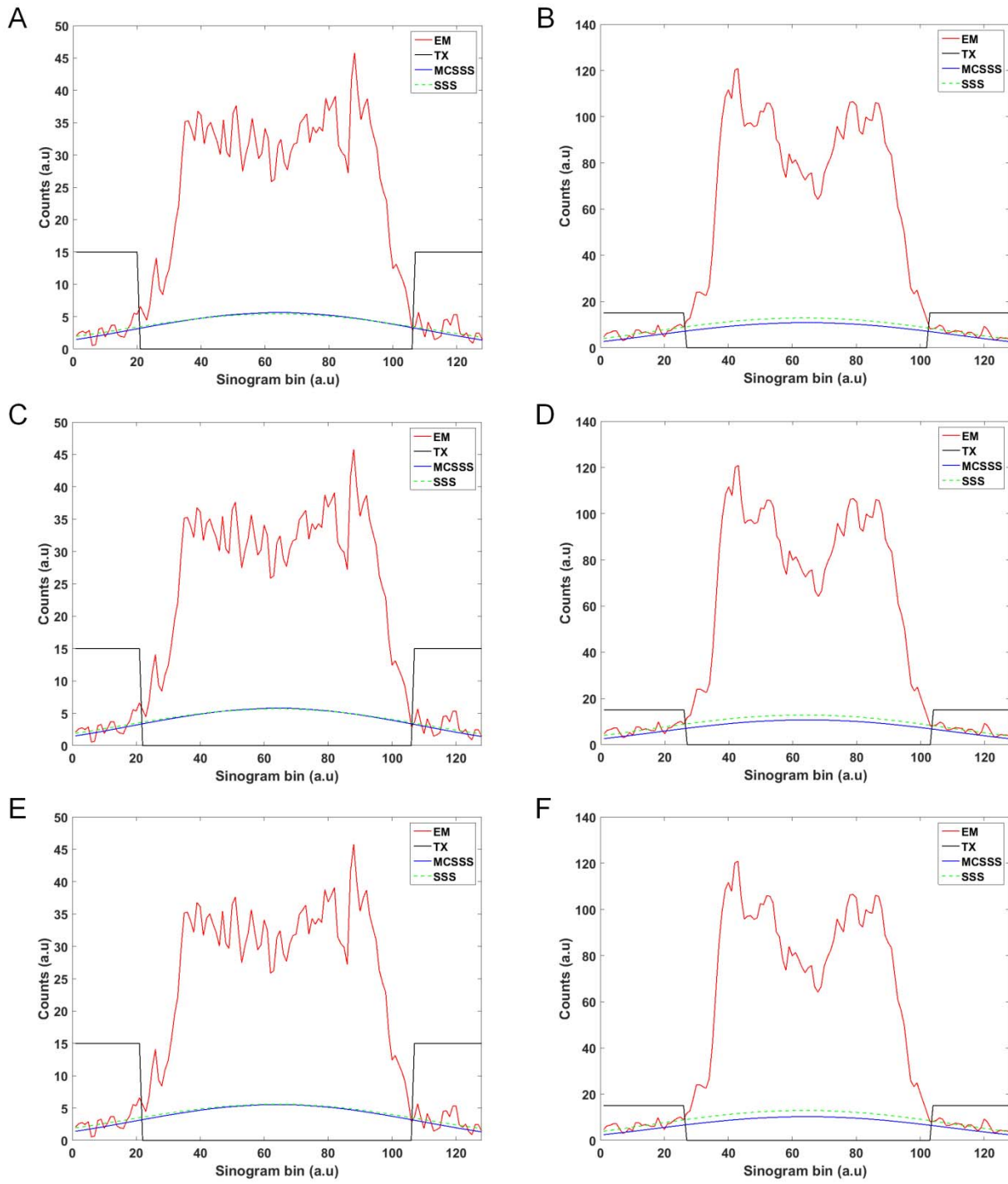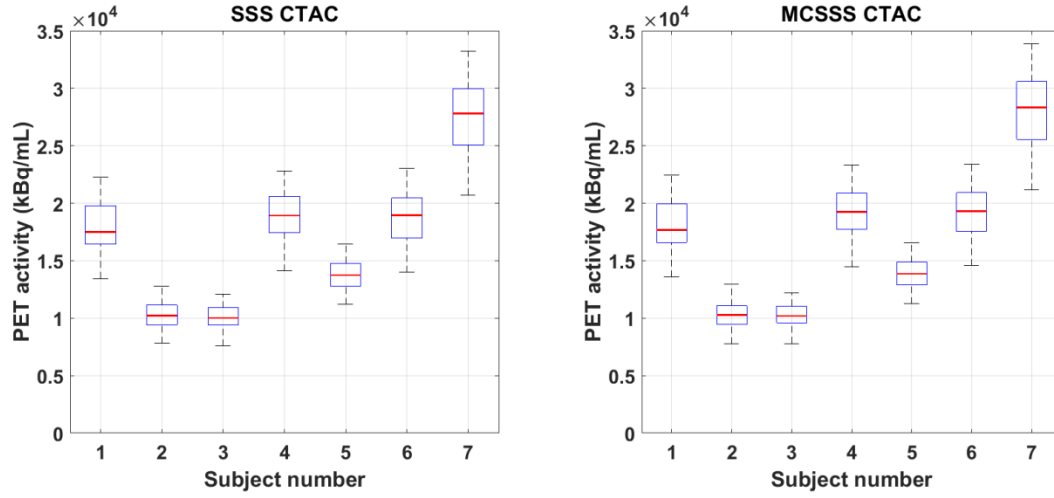
FIGURE 3. Measured sinogram profiles from randoms-corrected emission sinogram (EM) transmission sinogram mask (TX) and scatter sinograms form SSS and MCSSS for two subjects (number 4 and 1). The best (left column) and worst case showing poorer fit for MCSSS (right column) are presented. (A), (B) show CTAC, (C), (D) show MRAC$_{3class}$ and (E), (F) show MRAC$_{2class}$ reconstructed PET.
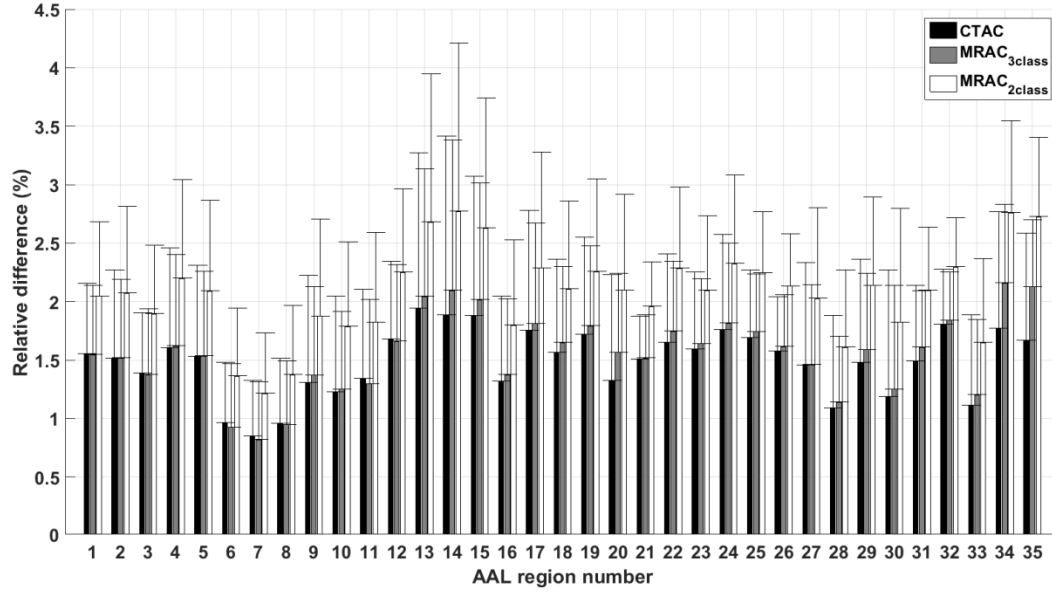
FIGURE 4. VOI analysis results of the subjects between SSS and MCSSS using different μ-maps. Regional differences between SSS and MCSSS remain the same regardless of the μ-map used (A) and remain small subject-wise as well (B). MCSSS results in higher reconstructed activity in (A) and (B) by 2 %. The largest differences exist with MRAC$_{2class}$. The anatomical regions are listed in Supplemental Table 1.
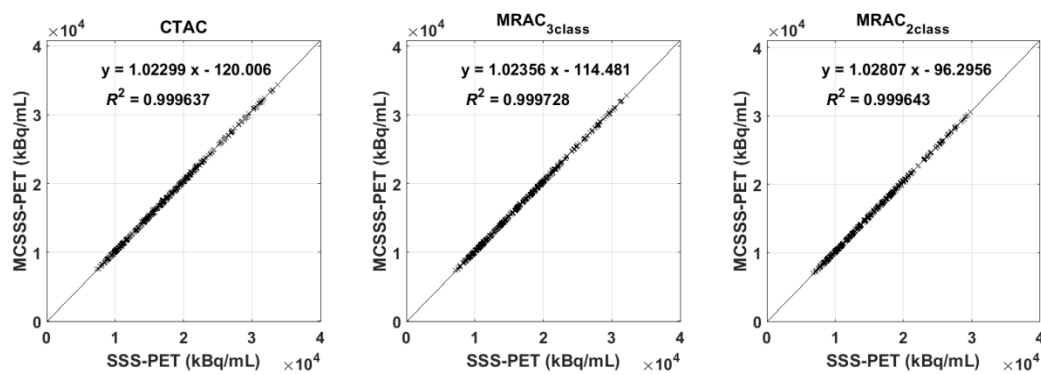
FIGURE 5. Linear regression plots from the clinical subjects. SSS and MCSSS reconstructed PET show excellent correlation ($R^2 > 0.99$), regardless of the μ-map used.
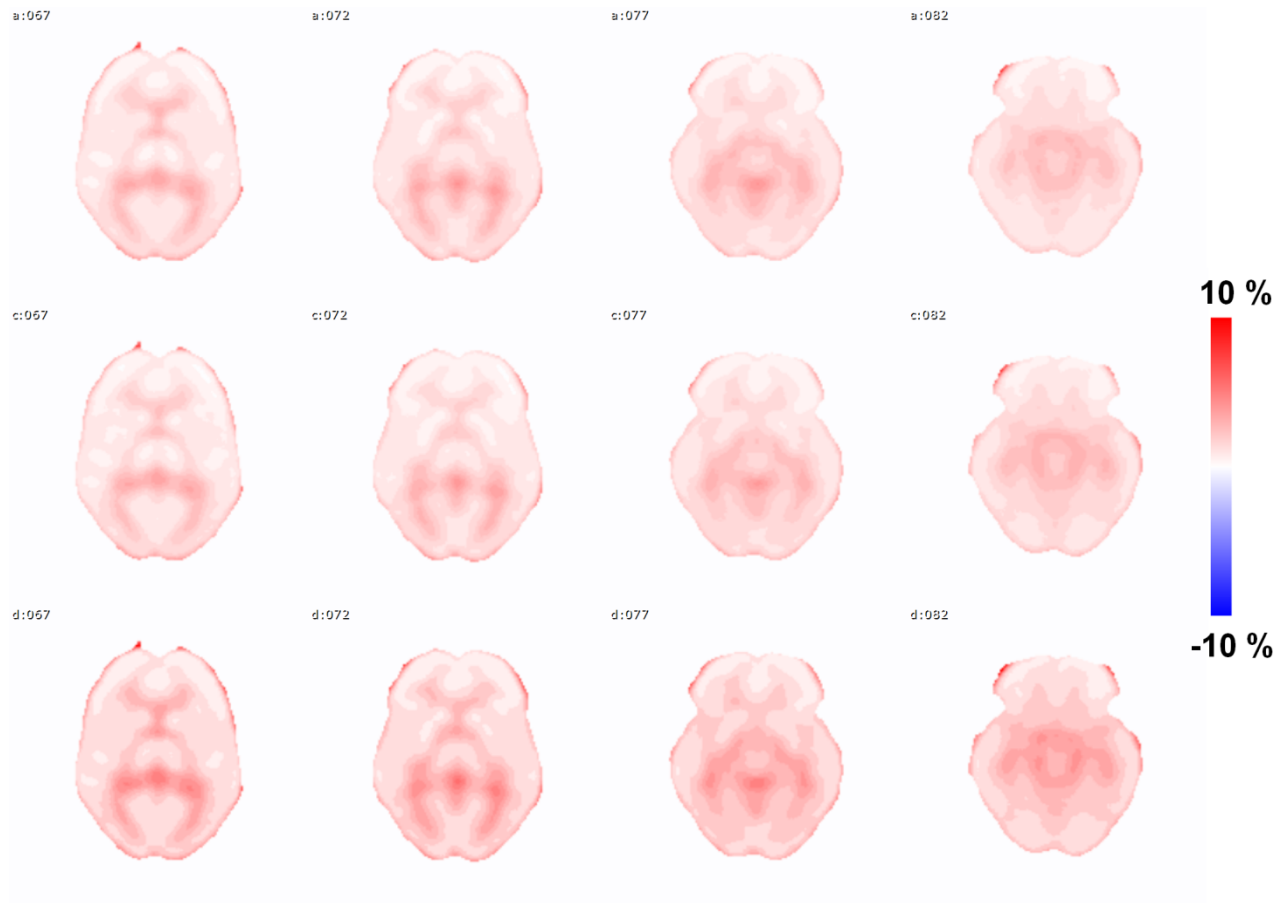
FIGURE 6. Mean ratio images calculated by equation (3) over all subjects, pixel-by-pixel comparison of SSS versus MCSSS. 1st row shows CTAC reconstructed PET while 2nd and 3rd row show $MRAC_{3class}$ and $MRAC_{2class}$ reconstructed PET, respectively. A small positive bias (< 5 %) in MCSSS reconstructed PET can be detected, which is more pronounced with $MRAC_{2class}$.
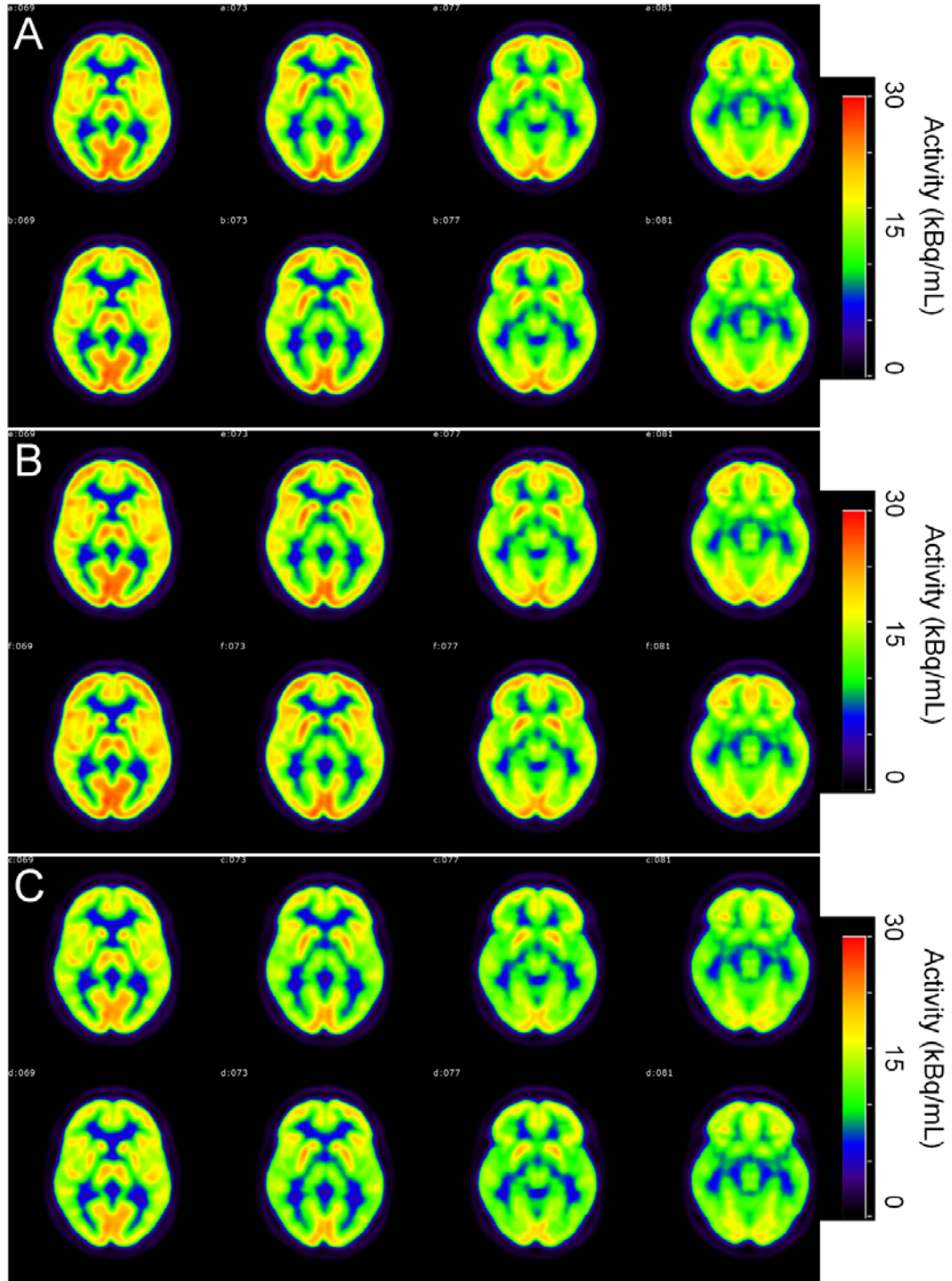
FIGURE 7. Mean PET images calculated over all subjects. (A) denotes CTAC reconstructed PET while (B) and (C) denote $MRAC_{3class}$ and $MRAC_{2class}$ reconstructed PET, respectively. The upper row of each subfigure denotes MCSSS reconstructed PET. No difference can be detected visually between SSS and MCSSS reconstructed PET images.

TABLES

<table>
<tr><td colspan="11">TABLE 1.
Calculated scatter fractions in (%) for each subject from equation (1).</td></tr>
<tr><td>μ-map</td><td>Scatter Algorithm</td><td>Subject 1</td><td>Subject 2</td><td>Subject 3</td><td>Subject 4</td><td>Subject 5</td><td>Subject 6</td><td>Subject 7</td><td>Mean±Standard deviation</td></tr>
<tr><td rowspan="2">CTAC</td><td>SSS</td><td>23.54</td><td>22.83</td><td>23.59</td><td>22.41</td><td>22.43</td><td>24.61</td><td>23.82</td><td>23.32±0.75</td></tr>
<tr><td>MCSSS</td><td>19.33</td><td>20.72</td><td>20.37</td><td>20.99</td><td>20.52</td><td>20.48</td><td>20.39</td><td>20.40±0.48</td></tr>
<tr><td rowspan="2">MRAC$_{3class}$</td><td>SSS</td><td>23.64</td><td>22.73</td><td>23.84</td><td>22.11</td><td>22.48</td><td>24.10</td><td>23.98</td><td>23.27±0.75</td></tr>
<tr><td>MCSSS</td><td>18.85</td><td>20.01</td><td>20.25</td><td>21.52</td><td>20.11</td><td>20.47</td><td>20.54</td><td>20.25±0.74</td></tr>
<tr><td rowspan="2">MRAC$_{2class}$</td><td>SSS</td><td>23.58</td><td>22.45</td><td>23.59</td><td>21.59</td><td>22.30</td><td>24.05</td><td>23.53</td><td>23.01±0.83</td></tr>
<tr><td>MCSSS</td><td>17.77</td><td>18.80</td><td>18.81</td><td>20.18</td><td>18.70</td><td>19.04</td><td>19.29</td><td>18.94±0.67</td></tr>
</table>

TABLE 2.

Measured activity values (kBq/ml) from the whole brain VOI with %RC calculated by equation (2).

| μ-map	Scatter Algorithm	Mean (kBq/ml)	Standard Deviation (kBq/ml)	Maximum (kBq/ml)	Recovery Coefficient (%)
CTAC	SSS	20.24	11.47	56.06	38.58
	MCSSS	20.17	11.48	56.08	38.43
	Difference (%)	-0.35	0.09	0.04	
MRAC$_{3class}$	SSS	18.07	10.43	51.16	34.43
	MCSSS	18.00	10.42	51.07	34.30
	Difference (%)	-0.39	-0.10	-0.18	
MRAC$_{2class}$	SSS	17.33	10.01	48.13	33.03
	MCSSS	17.44	10.02	48.26	33.23
	Difference (%)	0.63	0.10	0.27	

TABLE 3.

Calculated %RC (equation 2) of regional VOI in the phantom for CTAC reconstructed PET.

Scatter Algorithm	Medial Frontal Cortex	Lateral Frontal Cortex	Orbito-Frontal Cortex	Temporal Cortex	Cerebellum	Centrum Semiovale	Basal Ganglia	Cingulate Cortex	Mean	Standard Deviation
SSS	65.50	64.92	50.34	57.49	68.23	9.62	59.49	66.77	55.29	18.13
MCSSS	65.28	64.77	50.07	57.32	68.16	9.44	59.16	66.53	55.09	18.13

TABLE 4.

Calculated relative difference %Δ (equation 3) of the regional VOI in the brain phantom between SSS and MCSSS for each μ-map.

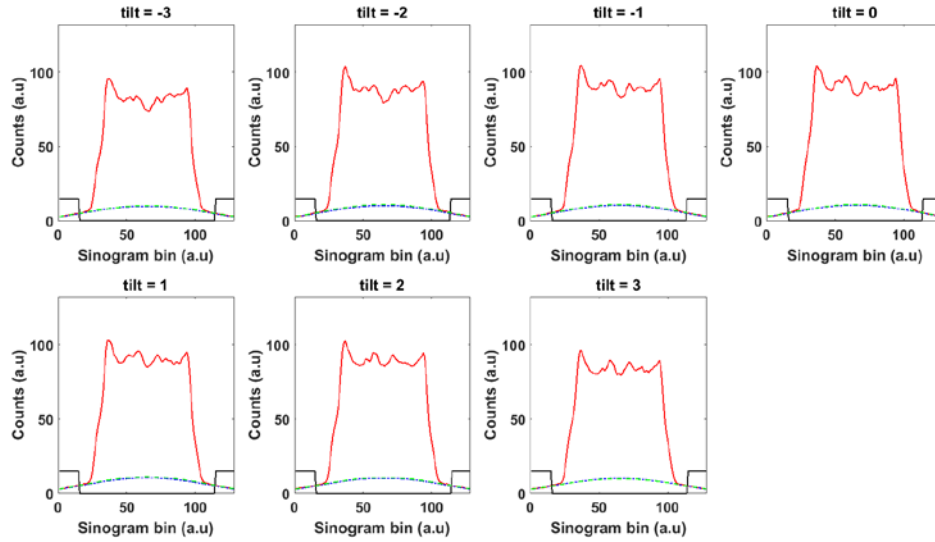| μ-map	Medial Frontal Cortex	Lateral Frontal Cortex	Orbito-Frontal Cortex	Temporal Cortex	Cerebellum	Centrum Semiovale	Basal Ganglia	Cingulate Cortex	Mean	Standard Deviation
CTAC	-0.34	-0.23	-0.53	-0.29	-0.11	-1.77	-0.56	-0.36	-0.52	0.49
MRAC 3class	0.27	0.20	0.09	0.33	0.38	1.46	0.34	0.34	0.42	0.40
MRAC 2class	0.45	0.33	0.29	0.49	0.53	2.51	0.61	0.55	0.72	0.68
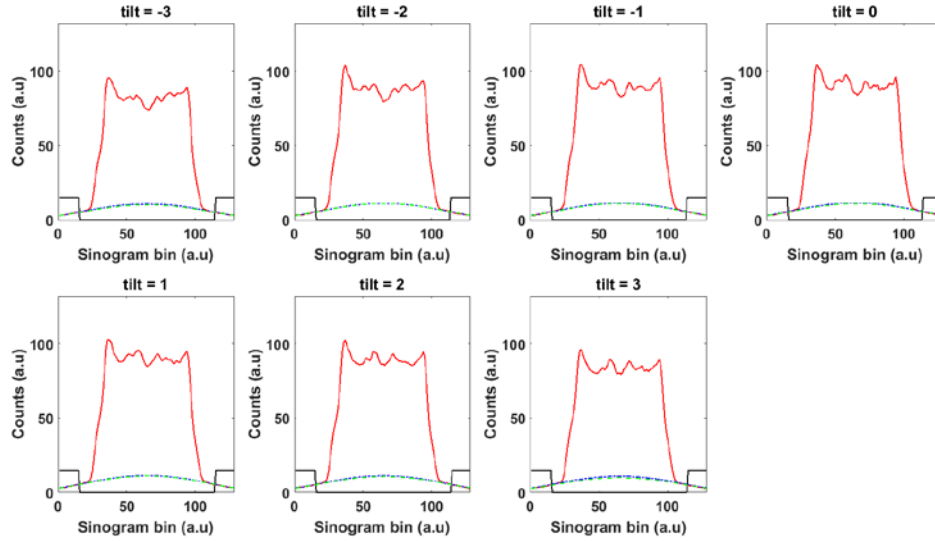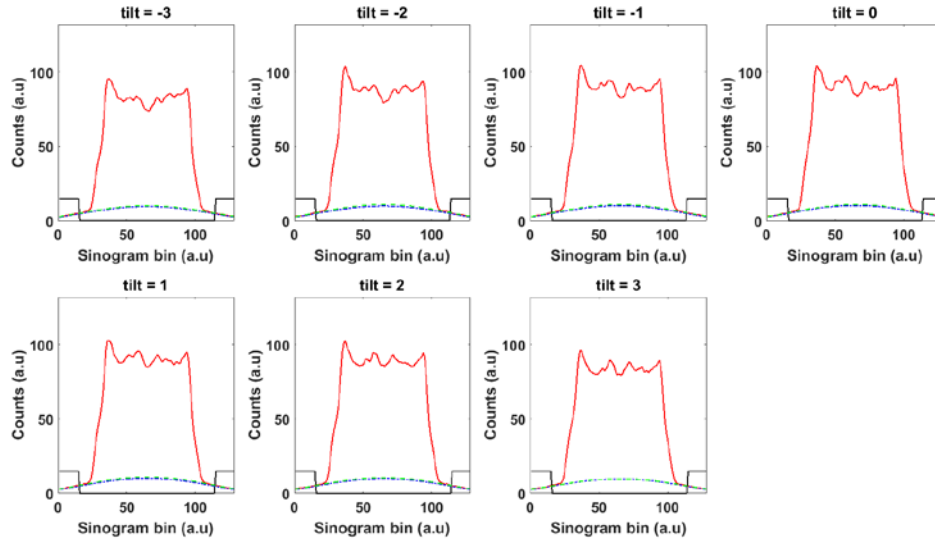
SUPPLEMENTAL FIGURE 1. Measured sinogram profiles of each individual tilt angle (N=7, from -3 to 3) when using CTAC and MRAC from the phantom study. For each tilt, the sinograms were averaged over all phi angles and the radial profile was plotted over the central axial bin. (A) shows the sinogram profiles for CTAC, (B) shows the sinogram profiles for $MRAC_{2class}$ and (C) shows the sinogram profiles for $MRAC_{3class}$. The red line denotes randoms-corrected emission

sinogram, the black line denotes transmission mask boundaries, while the green and blue lines denote SSS and MCSSS scatter correction sinograms for each algorithm, respectively. Only a small difference can be detected between the scatter sinograms regardless of the attenuation correction method. The smallest difference is achieved when using CTAC.
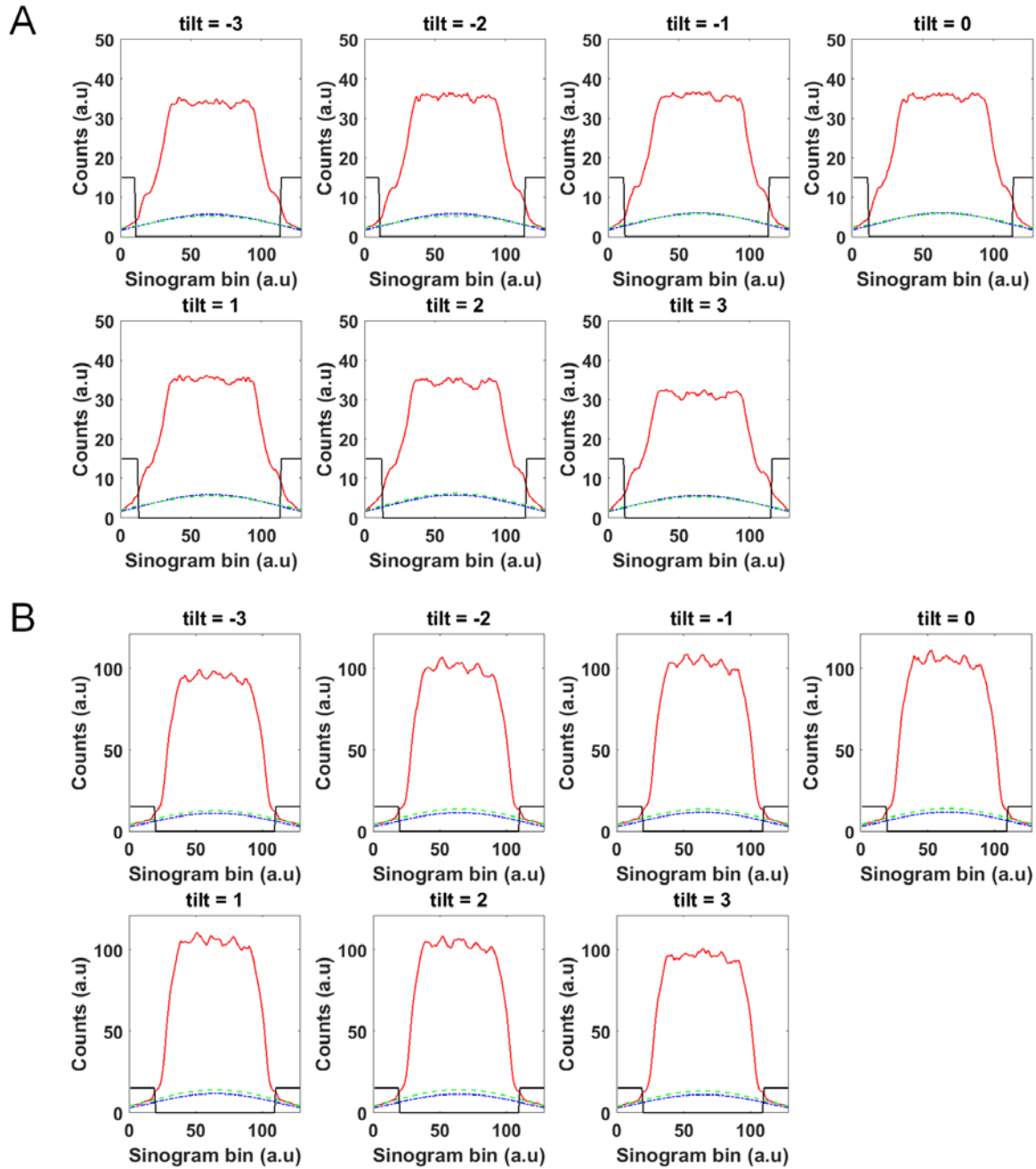
SUPPLEMENTAL FIGURE 2. Sinogram profiles from two clinical subjects (cases 4 and 1) presenting the smallest (A) and largest (B) detected difference between SSS and MCSSS algorithms with CTAC reconstructed PET data. Each individual tilt angle (N=7, from -3 to 3) is presented in a subplot. The sinograms were averaged over all phi angles and the radial profile was plotted over the central axial bin. (A) shows the sinogram profiles for the best case (smallest difference between SSS and MCSSS) subject and (B) shows the sinogram profiles for the worst case (largest difference between SSS and MCSSS) subject. In (B), MCSSS shows a poorer fit compared to SSS. The red line denotes randoms-corrected emission sinogram, the black line denotes transmission mask boundaries, while the green and blue lines denote SSS and MCSSS scatter correction sinograms for each algorithm, respectively.
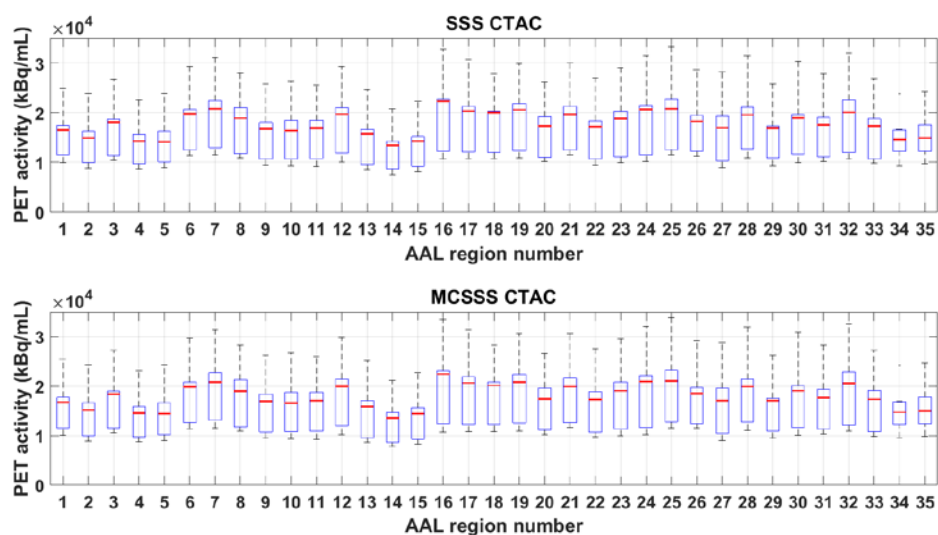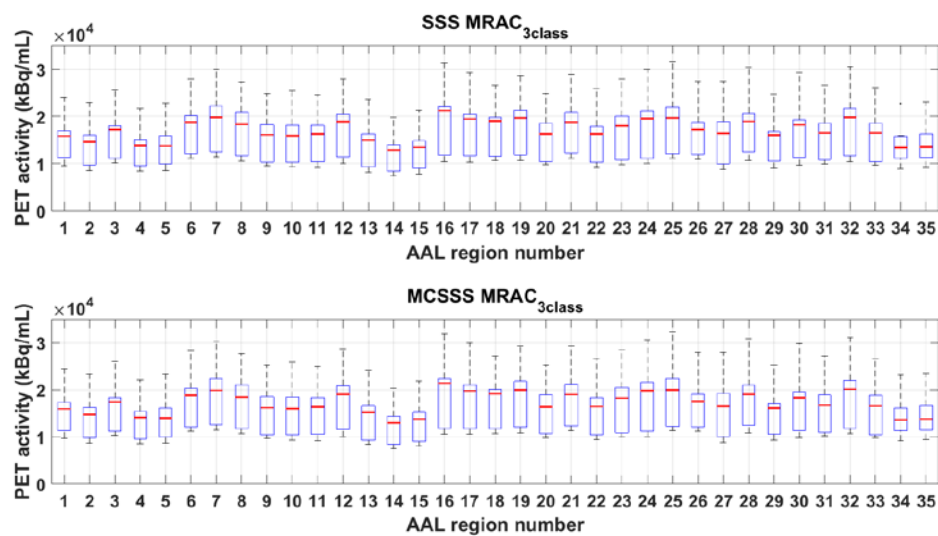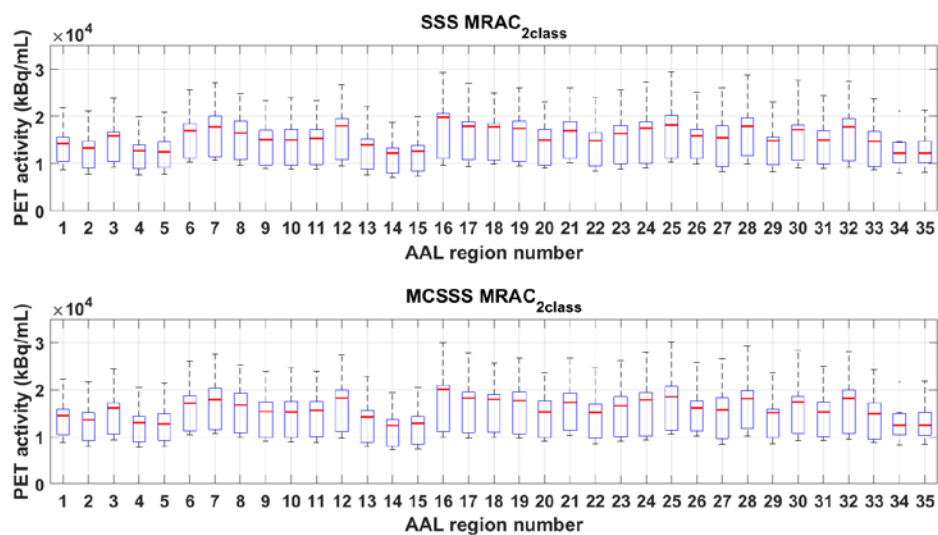
SUPPLEMENTAL FIGURE 3. Boxplots of individual VOI (35 VOI over 7 patients) with both scatter correction methods using CTAC (A), MRAC$_{2class}$ (B) and MRAC$_{3class}$ (C). The red line denotes the median activity, the edges of the box are the 25th and 75th percentiles, the whiskers denote the minimum and maximum activity, while individual outliers are defined by a black dot. MCSSS results in slightly higher activity compared to SSS, although the differences between MCSSS and SSS are small regardless of the attenuation correction method.

SUPPLEMENTAL TABLE 1.

Anatomical region numbers and their corresponding names as given in the AAL atlas.

Region Number	Region name		Region Number	Region name
1	Precentral		18	Lingual
2	Rolandic_Oper		19	Occipital
3	Supp_Motor_Area		20	Fusiform
4	Olfactory		21	Postcentral
5	(Region not named)		22	SupraMarginal
6	Frontal_Sup		23	Angular
7	Frontal_Mied		24	Precuneus
8	Frontal_Inf		25	Paracentral_Lobule
9	Rectus		26	Caudate
10	Insula		27	Putamen
11	Cingulum_Ant		28	Pallidum
12	Cingulum_Mid		29	Thalamus
13	Cingulum_Post		30	Heschl
14	Hippocampus/ParaHippocampal		31	Parietal
15	Amygdala		32	Temporal
16	Calcarine		33	Vermis
17	Cuneus		34	Cerebellum_Crus
			35	Cerebellum